OXFORD

Briefings in Bioinformatics, 2024, **25(2)**, 1–15
https://doi.org/10.1093/bib/bbad528
Problem Solving Protocol

MyoV: a deep learning-based tool for the automated quantification of muscle fibers

Shuang Gu†, Chaoliang Wen†, Zhen Xiao, Qiang Huang, Zheyi Jiang, Honghong Liu, Jia Gao, Junying Li, Congjiao Sun and Ning Yang

Corresponding author: Ning Yang, State Key Laboratory of Animal Biotech Breeding and Frontier Science Center for Molecular Design Breeding, National Engineering Laboratory for Animal Breeding, China Agricultural University, Beijing 100193, China. E-mail: nyang@cau.edu.cn

†Shuang Gu and Chaoliang Wen contributed equally to this work.

Abstract

Accurate approaches for quantifying muscle fibers are essential in biomedical research and meat production. In this study, we address the limitations of existing approaches for hematoxylin and eosin-stained muscle fibers by manually and semiautomatically labeling over 660 000 muscle fibers to create a large dataset. Subsequently, an automated image segmentation and quantification tool named MyoV is designed using mask regions with convolutional neural networks and a residual network and feature pyramid network as the backbone network. This design enables the tool to allow muscle fiber processing with different sizes and ages. MyoV, which achieves impressive detection rates of 0.93–0.96 and precision levels of 0.91–0.97, exhibits a superior performance in quantification, surpassing both manual methods and commonly employed algorithms and software, particularly for whole slide images (WSIs). Moreover, MyoV is proven as a powerful and suitable tool for various species with different muscle development, including mice, which are a crucial model for muscle disease diagnosis, and agricultural animals, which are a significant meat source for humans. Finally, we integrate this tool into visualization software with functions, such as segmentation, area determination and automatic labeling, allowing seamless processing for over 400 000 muscle fibers within a WSI, eliminating the model adjustment and providing researchers with an easy-to-use visual interface to browse functional options and realize muscle fiber quantification from WSIs.

Keywords: muscle fiber; deep learning; cell segmentation; MyoV; automatic quantification

INTRODUCTION

Skeletal muscle comprising ∼40% of the body's mass is the largest tissue in the human body, which is extensively distributed throughout [1]. Human movement relies on the contraction and extension of skeletal muscles; hence, the muscle tissue deterioration results in weakened physical strength and limited mobility, a condition known as sarcopenia [2–6]. This condition is characterized by the loss of muscle fibers and a decrease in the muscle cross-sectional area (CSA). In agricultural animal species, such as poultry, livestock and fish, the skeletal muscle serves as a valuable protein source for human nutrition [7, 8]. It is primarily composed of muscle fibers, of which characteristics play vital roles in the development and maintenance of the skeletal muscle function [9]. Therefore, exploring the development of muscle fibers is greatly important in the fields of human medicine and animal production [10].

Muscle fibers are elongated, multinucleated cells originating from the fusion of numerous mononucleated muscle precursor cells known as myoblasts during embryonic and fetal development [11–13]. The number of muscle fibers is believed to remain constant after birth [14]. Postnatal muscle growth and development mainly occur through two mechanisms, namely hypertrophy and regeneration, which involve protein synthesis and an increase in myonuclear hyperplasia [15, 16]. The assessment of muscle fiber development primarily relies on morphology,

Shuang Gu is a PhD candidate at the Department of Animal Genetics and Breeding, College of Animal Science and Technology, China Agricultural University. Her research mainly focuses on utilizing deep learning for the analysis of myofiber characteristics in animals.
Chaoliang Wen, PhD, is an Associate Professor at the Department of Animal Genetics and Breeding, College of Animal Science and Technology, China Agricultural University. His research interests mainly focus on the molecular mechanism underlying poultry economic traits and the innovation of breeding technologies.
Zhen Xiao is a Master at School of Computer and Information, Hefei University of Technology.
Qiang Huang is a PhD candidate at the Department of Animal Genetics and Breeding, College of Animal Science and Technology, China Agricultural University.
Zheyi Jiang is a Master candidate at the Department of Animal Genetics and Breeding, College of Animal Science and Technology, China Agricultural University.
Honghong Liu is a Master at the Department of Animal Genetics and Breeding, College of Animal Science and Technology, China Agricultural University.
Jia Gao is a Master candidate at the Department of Animal Genetics and Breeding, College of Animal Science and Technology, China Agricultural University.
Junying Li is a Senior Live stock Pastor at the Department of Animal Genetics and Breeding, College of Animal Science and Technology, China Agricultural University.
Congjiao Sun, PhD, is an Associate Professor of the Department of Animal Genetics and Breeding, College of Animal Science and Technology, China Agricultural University.
Ning Yang, PhD, is a Chair Professor of China Agricultural University and the Director of the National Engineering Laboratory for Animal Breeding. His research interests primarily focus on the genetic basis of economic traits in poultry and the innovation of breeding technologies and chicken breeds.
Received: September 25, 2023. **Revised:** December 6, 2023. **Accepted:** December 15, 2023

encompassing factors such as quantity, density and CSA [17, 18]. The accurate quantification of the muscle fiber phenotype is critical in investigating muscle development.

Several tools are available for quantifying the histological characteristics of muscle fibers after staining and divided into the two categories of manual and automated measurement methods using image processing software, such as ImageJ and Image-Pro Plus. However, manual measurement can be time-consuming and subjective due to interobserver variations [19, 20]. Automatic measurement is generally based on random fields of local microscope images [21] that do not fully represent the entire muscle fiber morphology and may equally be responsible for large errors. For whole slide images (WSIs) of the muscle, current methods are inefficient because of the vast quantity of muscle fibers numbering in the tens of thousands [22]. Some studies have proposed an estimation method for determining the total number of muscle fibers (TNM). This method involves selecting several local fields of view within a whole muscle slice to calculate the average density of the muscle fibers. The average density is then multiplied by the slice area to obtain the TNM estimate [23]. This approach leads to inaccuracies because the average density of the local field of view cannot replace the average density of the entire panorama.

Furthermore, existing tools primarily focus on muscle images in the hypertrophy phase [24] and lack accuracy in automatically measuring the muscle fiber boundaries in the early stages of muscle development. Therefore, current image processing techniques must be integrated into the fields of biology and medicine to devise methods applicable to all developmental stages and precisely and automatically quantify entire slices [25, 26]. The rapid progress of artificial intelligence has led to the widespread adoption of deep learning in biomedical fields, particularly in image recognition and semantic segmentation [27, 28]. For example, Li *et al.* [22] proposed the deep convolutional neural network that is effective in measuring the muscle fiber cross-sections in histopathological images and faces various challenges, such as low signal-to-noise ratio, uneven background and close adjacency between muscle fibers. In addition, the U-Net [29] architecture has emerged as a prominent segmentation benchmark, inspiring the development of various improved models, including k-U-Net [30], three-dimensional deep convolutional neural networks [31], fully convolutional neural networks [32] and deep neural networks [33]. Notably, StarDist [34] is a convolutional neural network that utilizes star-shaped convex polygons for cell nuclei localization. It can accurately locate and segment cell nuclei by learning to segment object boundaries and shapes, performing well in cell segmentation tasks. Recent years have witnessed the development of several tools for cell segmentation based on these techniques. Some notable examples include CellProfiler [35], ilastik [36], Cellpose [37], DeepImageJ [38] and ZeroCostDL4Mic [39], which offer advanced algorithms for image analysis, segmentation, classification, counting, tracking and training deep learning models.

Aside from the abovementioned algorithms and software, the development of various ImageJ plug-ins has facilitated the analysis of the muscle fiber histology. These plug-ins offer a wide range of features, including the ability to quantify the muscle fiber CSA, the number of nuclei, the number of satellite cells and the muscle fiber types of normal and regenerated muscles. Some of the most popular plug-ins include MuscleJ [40], Open-CSAM [41], MyoSAT [42], Myosoft [43] and MyoView [44]. While these tools offer valuable insights for determining the muscle fiber histological indicators, importantly, they are primarily crafted for analyzing immunofluorescence muscle slices, rather than being specifically designed for analyzing hematoxylin and eosin (H&E)-stained muscle slices. The analysis of H&E-stained muscle slices using ImageJ software has limitations primarily caused by their susceptibility to variations in the slide staining quality and the need for manual adjustment parameters. These adjustments can be time-consuming and prone to error [45, 46]. In addition, cell segmentation tools for H&E-stained muscle sections, such as Charisma [47], Cellpose [37] and MyoSAT [42], have several key limitations. First, training datasets are small, resulting in the capture of limited image information and low accuracy rates. Second, the stability and universality of these tools are affected by the number of muscle fibers in the muscle sections. In other words, their predicted results may significantly differ from the ground truth when dealing with slices containing a large or small number of muscle fibers. Third, these tools are time-consuming when quantifying slices on a large scale. For example, it takes ∼5 min for Charisma to process an image containing ∼300 muscle fiber cells [47]. Cellpose is a useful software for cell recognition and segmentation; however, quantifying the recognition cells requires additional image statistics tools, leading to an increased workload for the quantification process [37]. As an image processing plug-in for ImageJ, MyoSAT requires the manual adjustment of relevant parameters during runtime based on the characteristics of each muscle picture, making it unsuitable for large-scale applications [42].

In this study, we overcome these technique bottlenecks by collecting a substantial number of muscle slice samples from chickens at various developmental stages considering their short feeding cycle and ease of obtaining samples. The WSIs are cut into image tiles to magnify the muscle fiber images for better visualization and analysis. The accuracy of the training dataset annotations is ensured. Subsequently, we implement mask regions with convolutional neural networks (Mask-R-CNN) [48] with a residual network (ResNet-101) [49] and feature pyramid network (FPN) as the backbone network to develop an entirely automated image segmentation and quantification tool, called MyoV. This tool enables a precise quantification of the muscle fibers in H&E-stained muscle sections at any growth stage of model to farm animals. It eliminates the need for manual parameter adjustment during the quantification process, thereby reducing the need for manual intervention and improving the work efficiency. Furthermore, MyoV can automatically cut and quantify WSIs, making a large-scale muscle slice analysis more convenient and efficient than that of previous methods. To further enhance the user experience, MyoV has a user-friendly graphical interface that allows users to easily quantify the muscle fibers in H&E-stained muscle sections with a simple button click. Overall, MyoV is an accurate, efficient and user-friendly automated tool that provides a novel solution for muscle slice analysis and holds significant scientific research and application value.

RESULTS

Estimated TNM obtained by the estimation method significantly differed from the actual value

The TNM is a crucial indicator in muscle studies. The methods used to estimate the TNM involve selecting multiple local fields of view within a whole muscle slice to calculate the average density of the muscle fibers. Subsequently, the average dentistry is multiplied by the slice area to obtain an approximate TNM value. We compared the three following methods to assess the reliability of the estimation method for determining the TNM of the WSIs: estimation, semiautomatic and manual counting methods.

The semiautomatic method described herein involves manually partitioning WSIs into distinct regions that can be recognized by ImageJ, followed by utilizing ImageJ to detect the muscle fiber quantity. The semiautomatic and manual counting methods were first compared by quantifying two artificially divided images. The absolute number of the muscle fibers in No. 52 was 1210, with a difference of only −3.06% from the ImageJ result (Figure 1A). The exact muscle fiber quantity in No. 53 was 1625, depicting a difference of only 5.78% compared to the ImageJ result (Figure 1B).

The discrepancy between the semiautomatic and manual counting methods did not exceed 6.00%, suggesting that the semiautomatic method yielded more reliable results. We then compared the semiautomatic and estimation methods using a WSI of the early stages of the muscle fiber morphology. The pectoral muscles of young chickens were collected. The muscle histological sections were stained with H&E, and then panoramically scanned to obtain the WSI (Figure 1C). The WSI was magnified, and 10 partial fields of view were randomly exported at 400× magnification (Figure 1D). These 10 images were imported into ImageJ software to measure the average muscle fiber density, which we multiplied by the pectoralis major region area of the WSI to estimate the TNM, obtaining a value of 321 880 (Figure 1D). Meanwhile, the pectoral major muscle of the WSI was manually divided into 53 small regions. The TNM in these regions was calculated using ImageJ, which yielded a value of 254 691 (Figure 1E). The estimated method result was 26.38% higher than the semiautomatic method result.

Further research is needed to investigate whether the same discrepancy exists between methods using the WSIs of the mature stages of the muscle fiber morphology. We collected muscles from adult chickens and prepared H&E-stained slices to estimate the TNM using the two previously mentioned methods (Figure 1F). The estimation method produced a TNM of 60 820, while manually dividing the muscle into 13 regions and identifying them with ImageJ produced a TNM of 49 319 (Figure 1G and H). The large difference between the two methods (23.32%) suggested that the estimation method may have a larger error because the average density of several partial fields of view cannot represent the overall view.

Although manually dividing the WSIs into regions recognizable by ImageJ produced results closer to the actual value, this was not practical due to the time-consuming and labor-intensive procedures. Therefore, an accurate and simplified statistical method for the automatic segmentation and quantification of H&E-stained muscle fibers must be developed and applied in muscle development studies.

MyoV is an innovative muscle fiber analysis tool based on deep learning techniques

We propose herein an automated tool for quantifying muscle fibers with the WSIs of the muscle. This tool is called MyoV. The size of the WSIs is not a fixed value and depends on the size of the muscle slice sample. To retain the image features and finer details, the WSIs were cut into image tiles measuring 512 × 512 or 2048 × 2048 px as the input images. We utilized ResNet-101 and an FPN as the backbone neural network in this work (Figure 2). We extracted the feature maps by feeding the ResNet-101 + FPN backbone network with the image tiles to be detected. This network has two subsequent branches. The first branch, known as the region proposal network (RPN), sets specific candidate anchors at each feature point to serve as a proportional reference for the target size prediction. The RPN then filters and narrows down these anchors to obtain proposals that meet the needed standards. Region of Interest (ROI) Align was utilized to standardize the sizes of the feature maps and proposals to maintain consistency during later processing because the anchors' initial size is arbitrary.

We set different anchor scales according to the characteristics of different image categories. For example, images with larger muscle fibers need larger anchors (i.e. 16, 32, 64, 128 and 256), while images with smaller muscle fibers use smaller anchors more appropriately (i.e. 8, 16, 32, 64 and 128). Different feature map levels have different representational capabilities, with the shallow layer features reflecting details, such as light and dark, and the deeper layer features reflecting a richer overall structure. If only the shallow features are used to enhance the target detection capability, high-level semantic features will be lost. The model will also fail to make good predictions. Thus, a natural idea was to fuse deeper convolution and shallow features to obtain fused features with a richer expression. After processing, MyoV outputs segmented results, including the number and the CSA of muscle fibers.

Efficient processing of MyoV in different developmental stages

A total of 303 271 muscle fibers were manually or semiautomatically labeled to train a suitable model for the muscle fiber phenotype quantification, which we named Model_1 (Table S1). This training dataset comprised pectoral muscle slices from newly hatched chickens, in which the muscle fiber shape was still being formed, and the boundaries were not yet very clear. Nevertheless, obtaining muscle slices containing the TNM was easier at this stage, making it a special period. After birth, the muscle fibers began to undergo hypertrophy, resulting in clearer boundaries and a more mature shape. This period was significant for studying muscle development and damage; therefore, we divided the hypertrophy period into the two following stages based on the muscle fiber density: juvenile and mature. The training datasets for the juvenile and mature periods consisted of 294 578 and 65 490 muscle fibers, respectively (Table S1). The models trained using these two datasets were referred to as Model_2 and Model_3, respectively, with Model_3 being the most frequently used by researchers.

MyoV is a highly efficient tool that significantly enhances the image processing efficiency for muscle development phenotype assays. We conducted an experiment to measure the time needed for 30 WSIs to be cut and quantified by MyoV using a configuration of six cores and two accelerators in a high computing platform (Intel Xeon Ice Lake 6348, CPU@2.6 GHz × 2, NVIDIA HGX A100 40 GB × 8). Our findings showed that Model_1 can cut a WSI into 1083 image tiles (512 × 512 px) containing 333 624.90 muscle fiber cells with a CSA of 5.65 μm^2. Model_1 cut and quantified a WSI, necessitating times of 99.40 ± 9.63 and 295.50 ± 25.51 s, respectively. For an image tile with 100 muscle fiber cells, counting was completed in 0.0865 ± 0.0020 s (Table 1).

Model_2 of MyoV can cut a WSI into 599 image tiles (2048 × 2048 px) containing 307 635.30 muscle fiber cells with a CSA of 105.09 μm^2. The times needed to cut and quantify a WSI using Model_2 of MyoV were 1453.10 ± 77.44 and 1953.80 ± 104.61 s, respectively (Table 1). Meanwhile, Model_3 of MyoV can cut a WSI into 1162.40 image tiles (2048 × 2048 px) with 134 518.10 muscle fiber cells and a single muscle fiber CSA of 1132.19 μm^2. The times needed to cut and quantify a WSI using Model_3 was 1979.10 ± 260.59 and 1228.60 ± 210.74 s, respectively (Table 1). In conclusion, quantifying image tiles with many muscle fibers (e.g. ∼500) or those with a larger CSA of muscle fiber cells (e.g. >1000 μm^2) requires more time for quantification using

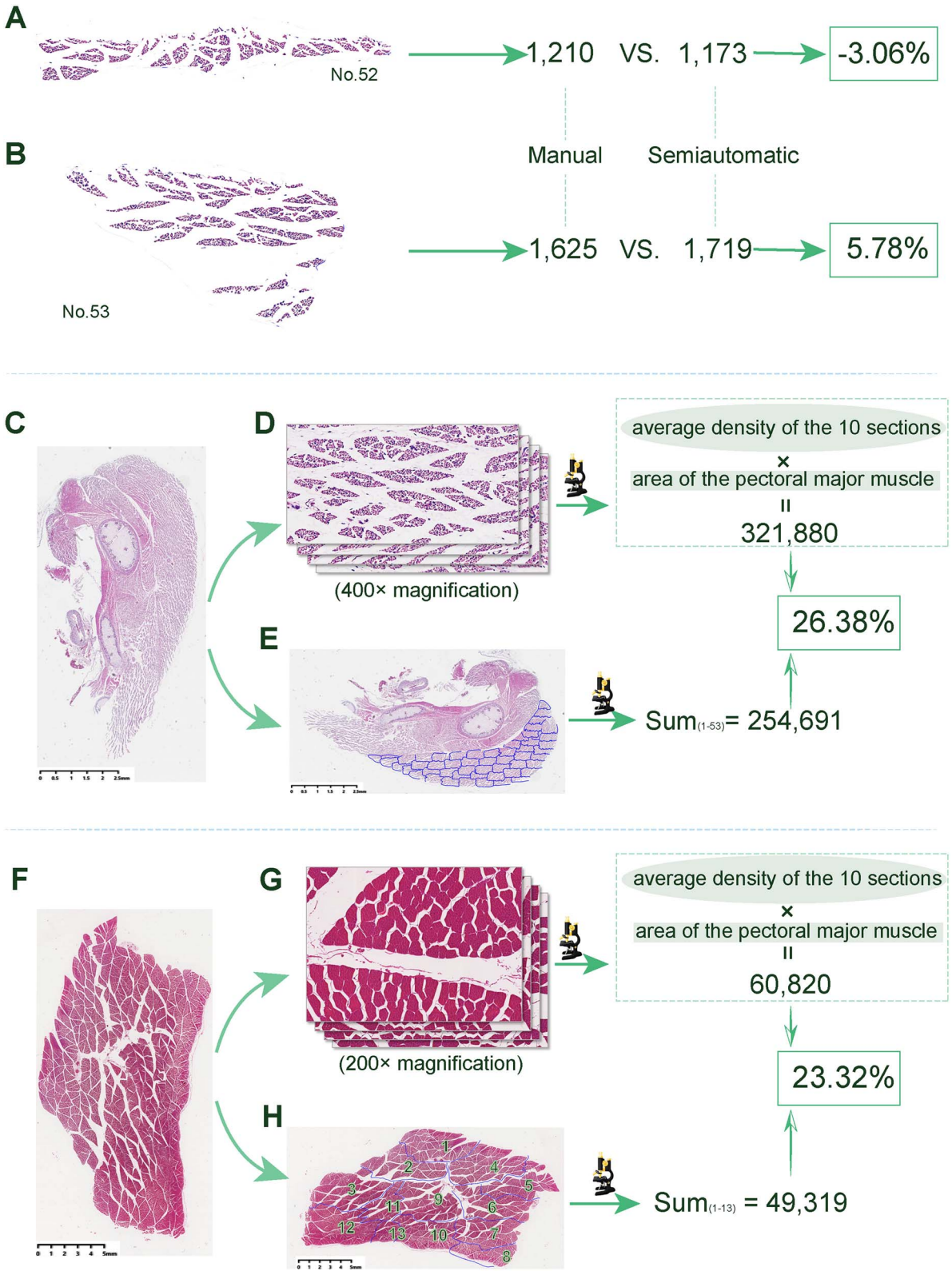

Figure 1. Exploration of the accurate determination of the TNM. (**A**) Region number 52 of (**E**) was selected to determine the number of muscle fibers with manual and semiautomatic counting. (**B**) Region number 53 of (**E**) was selected to determine the number of muscle fibers with manual and semiautomatic counting. (**C**) WSI of the chicken pectoral muscle at an early stage (1-day old). (**D**) Ten local fields of view of the pectoral muscle in a WSI randomly collected at 400× magnification and used to estimate the TNM. (**E**) Pectoral muscle in a WSI manually divided into 53 regions that can be identified in ImageJ software and TNM obtained by summing the number of muscle fibers in the 53 images. (**F**) WSI of a pectoral muscle of a chicken at the mature stage (72 weeks old). (**G**) Ten local fields of view of a WSI randomly collected at 200× magnification: a indicates the average density of the 10 sections, and b indicates the area of the pectoral muscle in the WSI used to estimate the TNM. (**H**) WSI manually divided into 13 regions that can be identified in ImageJ software and TNM obtained by summing the number of the muscle fibers in the 13 images.

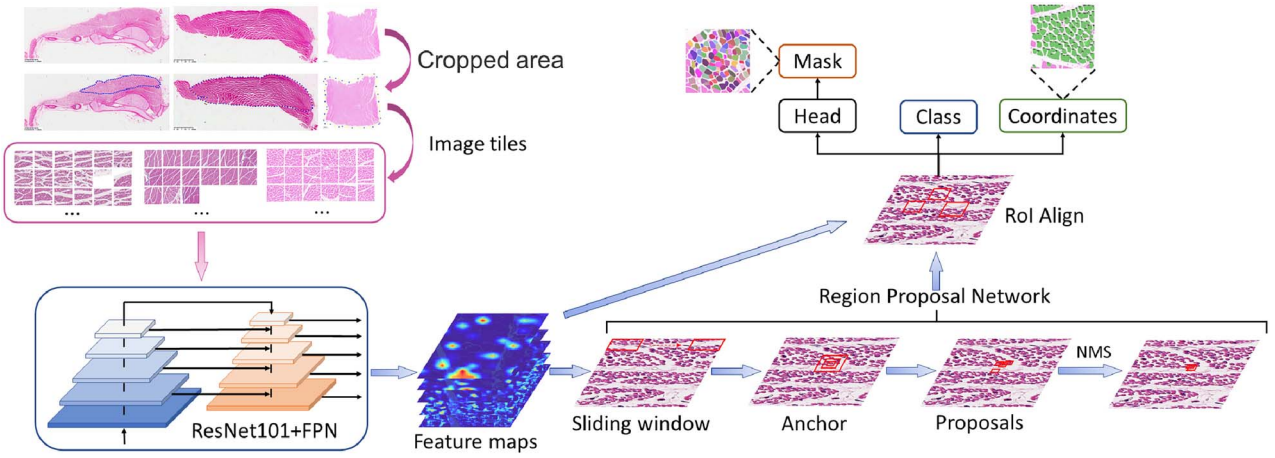

Figure 2. Flowchart of deep learning-based MyoV. The MyoV workflow was divided into several main procedures and one preparation procedure. In the preparation step, WSIs were cut into smaller image tiles (with dimensions of either 512 × 512 or 2048 × 2048 px) used as the input images for further muscle fiber cell detection. The main detection consisted of the following steps: first, each raw image tile was fed into the ResNet-101 + FPN backbone network to extract the feature map; next, the RPN set specific candidate anchor points at each feature point as a reference for target size prediction; the RPN then filtered and narrowed down these anchors to obtain proposals that meet the desired criteria; the initial anchor size was arbitrary; hence, ROI Align was used to normalize the sizes of the feature maps and proposals for consistency in postprocessing; and lastly, the results were obtained in two forms: muscle fiber cell count and muscle fiber cell area.

MyoV due to the relatively large particle size and the greater number of muscle fibers involved.

High performance of MyoV in muscle fiber quantification

Several conventional software options are currently available for detecting muscle fiber cells. In this study, we selected two software options, namely, the newly developed software Cellpose [37] and the classical image processing software ImageJ (Figure 3A–C).

The test dataset for Model_1 comprised newly formed muscle fibers observed during the postnatal period, with a small proportion of red cytoplasm and most blue nuclei. This dataset comprised 80 image tiles. For automated measurements, MyoV performed batch measurements, while Cellpose solely focused on cell segmentation, relying on other software for subsequent quantification tasks, which led to inconsistent detection results. ImageJ partially handled batches; however, significant variations were observed among images, necessitating manual parameter adjustments. The number of identified muscle fibers was also lower than the ground truth (Figure 3A). For image tiles containing fewer than 600 muscle fibers, the detection rate (DR) of MyoV was 0.95, surpassing the rates of 0.90 for Cellpose and 0.76 for ImageJ. The overall DR of the MyoV test dataset was 0.91, which was the highest among the three methods (Table 2). The test dataset for Model_2 consisted of 62 image tiles each containing many muscle fibers. Notably, 83.87% of the images contained more than 600 muscle fibers. The results evidently showed that MyoV performed significantly better with larger images. The prediction results closely aligned with the ground truth (Figure 3B). The overall DR was 0.94, which was significantly higher than those of Cellpose and ImageJ (Table 2). This discrepancy might be attributed to the relatively low prediction stability of the latter two software programs because a poor prediction accuracy was observed when the muscle fiber boundary was unclear (Figure 3B). In the Model_3 test dataset, the CSA of the muscle fibers was much larger than that in the two aforementioned test datasets, while the number of muscle fibers in a single image tile was significantly lower. The boundaries between the muscle fibers were clearly distinguishable, leading to MyoV achieving a DR of 0.96 and Cellpose and ImageJ having lower DRs of 0.80 and 0.87, respectively (Table 2) and exhibiting unstable performances (Figure 3C). Model_3 demonstrated an exceptional performance, offering an effective solution for the majority of scientific researchers involved in muscle fiber phenotype determination. Cellpose displayed some lower counts in Figure 3B and C. After examination and evaluation, we found that this result was caused by the dense muscle fiber distribution and the lack of clear boundaries (Figure S1). The presence of numerous cracks within the muscle fibers also further obscured their boundaries, indicating that Cellpose might not have been adequately optimized for analyzing these specific tissue sections, thereby leading to a cell count underestimation.

In addition to contrasting against popular image processing software, we performed comparisons with two other cutting-edge segmentation algorithms: StarDist [34] and U-Net [29]. For the testing images, we matched the predictions of the StarDist and U-Net algorithms to the ground truth at different thresholds of matching precision based on the standard intersection-over-union (IoU) metric. We then evaluated the segmentation performance with standard metrics: precision, recall, accuracy and F1-score (Figure 3D–F). MyoV demonstrated a superior performance over these two algorithms across all threshold values when tested with the Model_1, Model_2 and Model_3 datasets (Table S1). Model_1 matched with an average precision of 0.91, surpassing StarDist and U-Net that only achieved accuracies of 0.86 and 0.75, respectively, at the commonly used IoU threshold of 0.5 (Figure 3D). Similarly, the results with the Model_2 and Model_3 test datasets were consistently closest to the ground truth. At a 0.5 IoU threshold, values of 0.97 and 0.92, respectively, were obtained, which were higher than 0.93 and 0.84 obtained with StarDist (Figure 3E) and significantly higher than 0.55 and 0.06 obtained with U-Net (Figure 3F). Moreover, MyoV showed a more substantial improvement in precision than that of other methods at higher thresholds. In addition, cracks were formed inside the muscle fibers during paraffin sectioning and H&E staining, making it difficult to detect muscle fibers with conventional methods. However, this can easily be solved with MyoV (Figure S2). These results indicate that MyoV can accurately capture complex muscle fiber shapes, surpassing previous methods in terms of expressiveness.

Table 1: Time taken to process WSIs with different models

Model	N	Image tiles/WSI	TNM/WSI	CSA (μm^2)	Time of cutting		Time of counting			
					s/WSI	s/image tile	s/WSI	s/image tile	s/myofiber cell	s/100 myofiber cells
Model_1	10	1083.70 ± 87.58	339 624.90 ± 25 447.36	5.65 ± 0.31	99.40 ± 9.63	0.0919 ± 0.0046	295.50 ± 25.51	0.27 ± 0.01	0.0009 ± 0.0000	0.0865 ± 0.0020
Model_2	10	599.10 ± 46.49	307 635.30 ± 15 273.50	105.09 ± 8.55	1453.10 ± 77.44	2.5724 ± 0.2769	1953.80 ± 104.61	3.33 ± 0.12	0.0063 ± 0.0000	0.6340 ± 0.0040
Model_3	10	1162.40 ± 136.01	134 518.10 ± 17 964.10	1132.19 ± 131.54	1979.10 ± 260.59	1.6633 ± 0.0920	1228.60 ± 210.74	1.05 ± 0.08	0.0103 ± 0.0016	1.0261 ± 0.1606

The third column indicates that a WSI can be divided into n image tiles. The image tiles in the Model_1 row have a pixel size of 512 × 512, while those in the Model_2 and Model_3 rows have a pixel size of 2048 × 2048.

MyoV is a powerful tool in the biomedical study of muscle development and pathology

Mice are an essential animal model for studying muscle development. Researchers often concentrate on leg muscles, such as the gastrocnemius, to investigate muscle atrophy or damage. To evaluate the suitability of the MyoV tool developed in this study for mouse muscle research, we collected the soleus (Sol), extensor digitorum longus (EDL), flexor digitorum longus (FDL), biceps femoris (BF), gastrocnemius (GAS) and tibialis anterior (TA) of three male C57BL/6 mice sacrificed at 8 weeks of age, all of which had similar body weights (Figures 4A and S3A). These six muscles from each mouse were fixed and embedded. Five uniform slices were then cut from each wax block and stained with H&E. The resulting slices were digitally scanned in a panoramic scanner to generate the WSIs.

After examining the WSIs, we noted that the muscle fiber morphology at this stage exhibited significant boundaries. Therefore, Model_3 of MyoV, which was specifically designed to assess this kind of muscle fiber phenotype, was selected. Consequently, the WSIs were cut into smaller image tiles measuring 2048 × 2048 px, enabling the TNM and CSA quantification. The visualization results demonstrated that MyoV can indeed accurately identify and segment individual muscle fiber cells (Figure 4B). We randomly selected 100 image tiles for testing and achieved a DR of 0.93 (Figure 4C) and a precision value of 0.93 when an IoU threshold of 0.5 was applied (Figure 4D). Using MyoV, we proceeded to measure the TNM and the CSA within the WSIs obtained from six different muscle sites. Subsequently, we mapped the variations in both the number and the CSA of the muscle fibers across distinct muscle regions (Figure 4E and F). The results exhibited significant differences in the TNM and the CSA among the six muscles ($P < 0.01$). Sol displayed the lowest TNM (498.73 ± 71.71), which was lower than those of EDL (896.53 ± 86.29), FDL (1291.20 ± 181.67), GAS (1580.20 ± 102.28), BF (1717.67 ± 198.09) and TA (1983.33 ± 215.83) (Figure 4E). Notably, Sol also exhibited the smallest CSA (1187.09 ± 69.83 μm^2), while BF exhibited the largest CSA (1851.67 ± 73.14 μm^2) (Figure 4F). In addition, BF and GAS presented the highest weights of 0.1409 ± 0.0054 and 0.1436 ± 0.0015 g, respectively (Figure S3B). Sol had the fewest total TNM and the smallest CSA; thus, its WSIs fell within the range that can be measured by the Model_2 of MyoV. MyoV directly recognized and segmented Sol, with the visualization results demonstrating a very high accuracy in terms of recognition (Figure S3C). In comparison to the local field of view slices, the WSIs were proven to be a more reliable method for investigating alterations in the muscle fiber number and the CSA in mice. Furthermore, MyoV provided a more comprehensive and accurate approach, facilitating related research endeavors.

A collection of muscle injury images was obtained through article retrieval. Representative images were selected. MyoV was utilized to predict the muscle fibers [50–59]. For images with a substantial number of muscle fibers, we employed Model_2 of MyoV for the measurement and discovered that repaired muscle fibers could accurately be identified (Figure 4G). This suggests that MyoV can directly recognize the WSIs containing clearly visible muscle fibers without the need for prior cutting and reidentification. In the case of repairing muscles, a significant number of immune cells can be observed, whereas we found only a few muscle fibers, which were uneven in size and did not fully recover to their normal shape (Figure 4H and I). Nevertheless, MyoV can accurately identify these muscle fibers using Model_3 of MyoV (Figure 4H). It can also identify and quantify the repaired

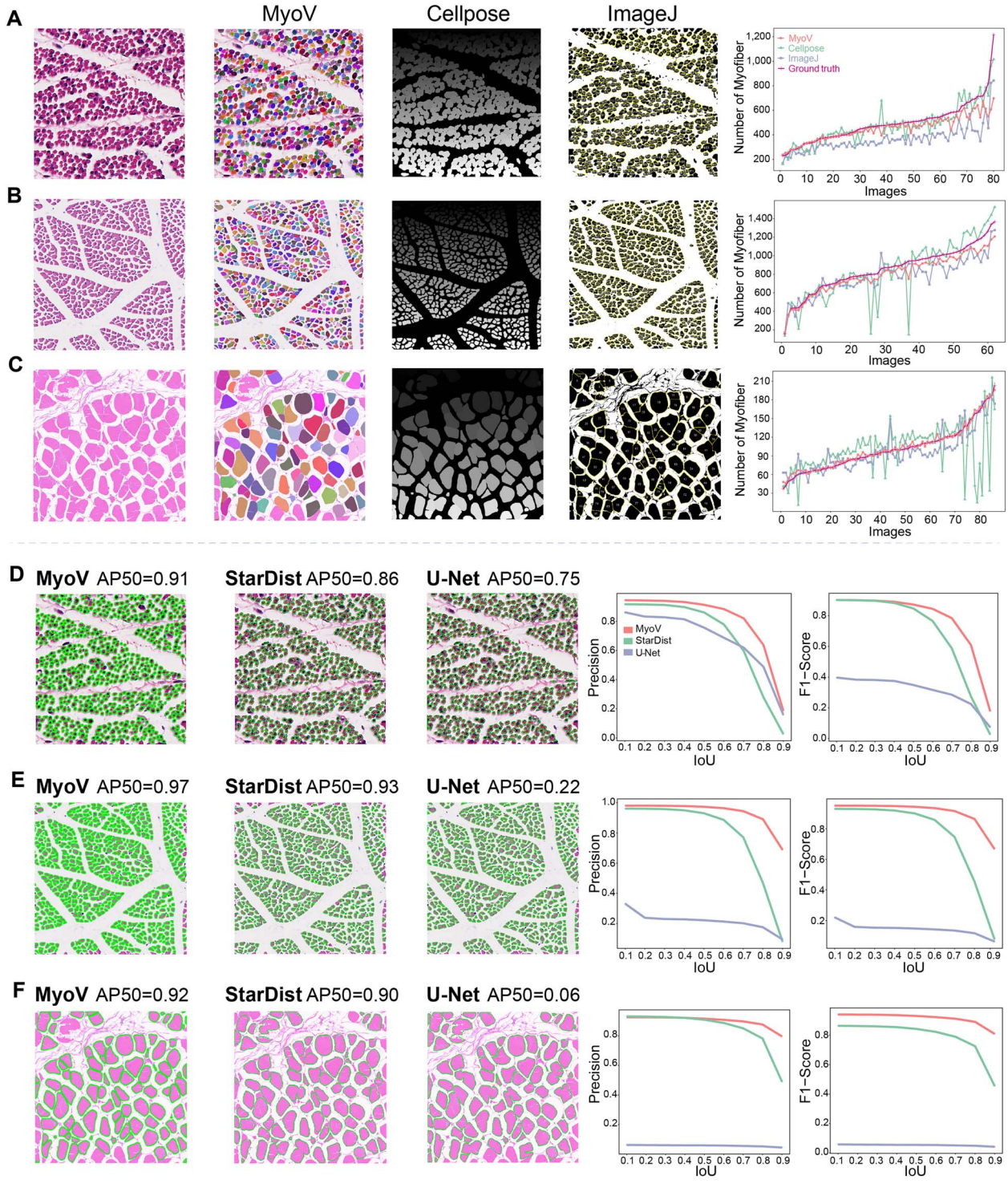

Figure 3. Segmentation performance of the three models. (**A**) Testing image segmentation for MyoV, Cellpose and ImageJ software and the DR of Model_1 with 80 testing images. (**B**) Testing image segmentation for MyoV, Cellpose and ImageJ software and the DR of Model_2 with 62 testing images. (**C**) Testing image segmentation for MyoV, Cellpose and ImageJ software and the DR of Model_3 with 86 testing images. (**D**) Example testing image segmentation for MyoV, StarDist and U-Net when trained as Model_1. The quantified performance of MyoV, StarDist and U-Net tested with Model_1 data ($n = 80$ testing images). The IoU threshold measured the similarity between the predicted and ground truth masks. A score of 1 indicated a perfect match, while 0.5 meant that there were as many correctly matched pixels as there were missed and false-positive pixels. The precision score was calculated based on the proportion of the matched and missed masks. (**E**) Example testing image segmentation for MyoV, StarDist and U-Net when trained as Model_2. Quantified performance of MyoV, StarDist and U-Net tested with Model_2 data ($n = 62$ testing images). (**F**) Example testing image segmentation for MyoV, StarDist and U-Net when trained as Model_3. Quantified performance of MyoV, StarDist and U-Net tested with Model_3 data ($n = 86$ testing images).

Table 2: Detection rate of MyoV compared with Cellpose and ImageJ software

Model	Ground truth	Images	Detection rate					
			MyoV		Cellpose		ImageJ	
Model_1	200–400	25	0.97	0.91	0.89	0.90	0.83	0.74
	401–500	21	0.96		0.91		0.74	
	501–600	21	0.92		0.90		0.72	
	601–1300	13	0.81		0.91		0.67	
Model_2	100–600	10	0.96	0.94	0.88	0.88	0.86	0.88
	601–900	25	0.94		0.87		0.91	
	901–1000	11	0.94		0.86		0.89	
	1001–1400	16	0.92		0.92		0.86	
Model_3	40–80	26	0.93	0.96	0.77	0.77	0.85	0.87
	81–100	23	0.97		0.76		0.88	
	101–120	17	0.97		0.85		0.87	
	121–210	20	0.98		0.69		0.88	

The second column indicates the number of the actual muscle fibers contained in an image.

muscle fibers in various slices after a muscle injury, irrespective of the color depth, immune cell presence or muscle fiber integrity (Figure 4I).

MyoV is an efficient and convenient tool for muscle fiber quantification in animal production

Livestock, such as poultry, pigs and cattle, are of great agricultural and economic importance because they provide humans with high-quality protein sources. By addressing the challenge of accurately quantifying the TNM, MyoV can assist breeders in efficiently developing new breeds of meat livestock and poultry that better fulfill human demands. In this study, we selected commercial white-feathered broiler chickens (Figure 5A) as an example and used images of chicken slices from different breeds. To obtain muscle slices containing all the pectoralis major muscle fibers, we trimmed the block along the collarbone until we reached the lateral midpoint (Figure 5B). Then, we used MyoV to extract image tiles from the WSIs, which were subsequently analyzed using MyoV to obtain the number of muscle fibers and the CSA. The resulting visualizations, displayed from left to right, represent the muscle fibers at D1 (postnatal day 1, the same below), D7 and D35 (Figure 5C). The experimental results demonstrated that MyoV can accurately identify individual muscle fibers, thereby ensuring the reliability of the findings obtained. Ducks are a type of waterfowl. Their direction of selection differs from that of chickens. While Peking ducks grow quickly, they have a comparatively lower skeletal muscle content. Specifically, at D1 and D7, the thigh muscles of Peking ducks developed significantly faster than the calf muscles, outpacing the pectoralis muscles (Figure S4). However, the quality of the duck breast muscle slices was not ideal. A test dataset of 20 images with unclear muscle fiber boundaries was randomly selected for Model_1 of MyoV (Figure 5D). A DR of 0.89 was then achieved (Figure 5E). At 0.5 IoU threshold, the precision and recall rates were 0.86 and 0.78, respectively (Figure 5F). For Model_2, duck leg muscle slices were used as a test dataset, with 50 randomly selected images (Figure 5G). The DR rate was 0.94 (Figure 5H). Consistent with the DR, the precision and recall rates of 0.96 and 0.94, respectively, were also high at a 0.5 IoU threshold (Figure 5I).

We conducted experiments using muscle slices from Beijing black pigs (D160–300) and Angus cattle (D56) to further validate the universality of our research method. The longissimus dorsi muscle, which is a vital part of the spinal ridge, holds great economic importance in the production of fresh meat products. For Model_2 of MyoV, we randomly selected 20 images as the test dataset (Figure 5J). Varying degrees of differences in the color and distribution uniformity of the slices can be found in this test dataset. The DR was 0.95 (Figure 5K), with 0.83 precision, 0.86 recall rate and 0.85 F1-score (Figure 5L). We randomly chose 50 images as the test dataset for Model_3 of MyoV (Figure 5M). The DR for this test dataset was 0.93 (Figure 5N), which was slightly lower than that for the Model_2 test dataset. However, the precision was 0.90, the recall rate was 0.93 and the F1-score was 0.91 (Figure 5O). These values were higher than those from the Model_2 test dataset. The muscle slices from the quadriceps femoris muscle of Angus cattle grown until D56 were suitable for the phenotype determination using Model_3 of MyoV. We randomly selected 35 images for this purpose (Figure 5P) and achieved a DR of 0.92 (Figure 5Q). Under the IoU threshold of 0.5, the precision and recall rates were 0.93 and 0.86, respectively (Figure 5R). Despite the significant differences in size and the varied quality of the slices from these livestock, MyoV had suitable models for accurately determining the muscle fiber phenotypes (Figure S5).

DISCUSSION

H&E staining is a commonly used and convenient method for studying muscle phenotypes in biological research and medical pathology and is particularly suitable for histological analysis [60–62]. However, the previously developed algorithm models for identifying H&E-stained cells are limited in terms of accuracy and running speed [37, 47]. This study presents a novel method of accurately counting the number of muscle fibers using deep learning techniques. Our proposed method is specifically designed for H&E-stained sections and has been developed into a user-friendly software that can easily be utilized by researchers without computer vision expertise.

We used three models with varying sizes of training datasets, ranging from 60 000 to 300 000 muscle fiber cells. Each contained a wide distribution of morphological characteristics, such as cell shape, color and size. The trained models demonstrated a superior performance with the test images compared to that of both U-Net and StarDist, indicating that the algorithms and the network architecture utilized herein were highly suitable for detecting the segmented H&E-stained muscle slices. The lower performance obtained with the U-Net method can be attributed to the absence of coordinate information, making it unsuitable

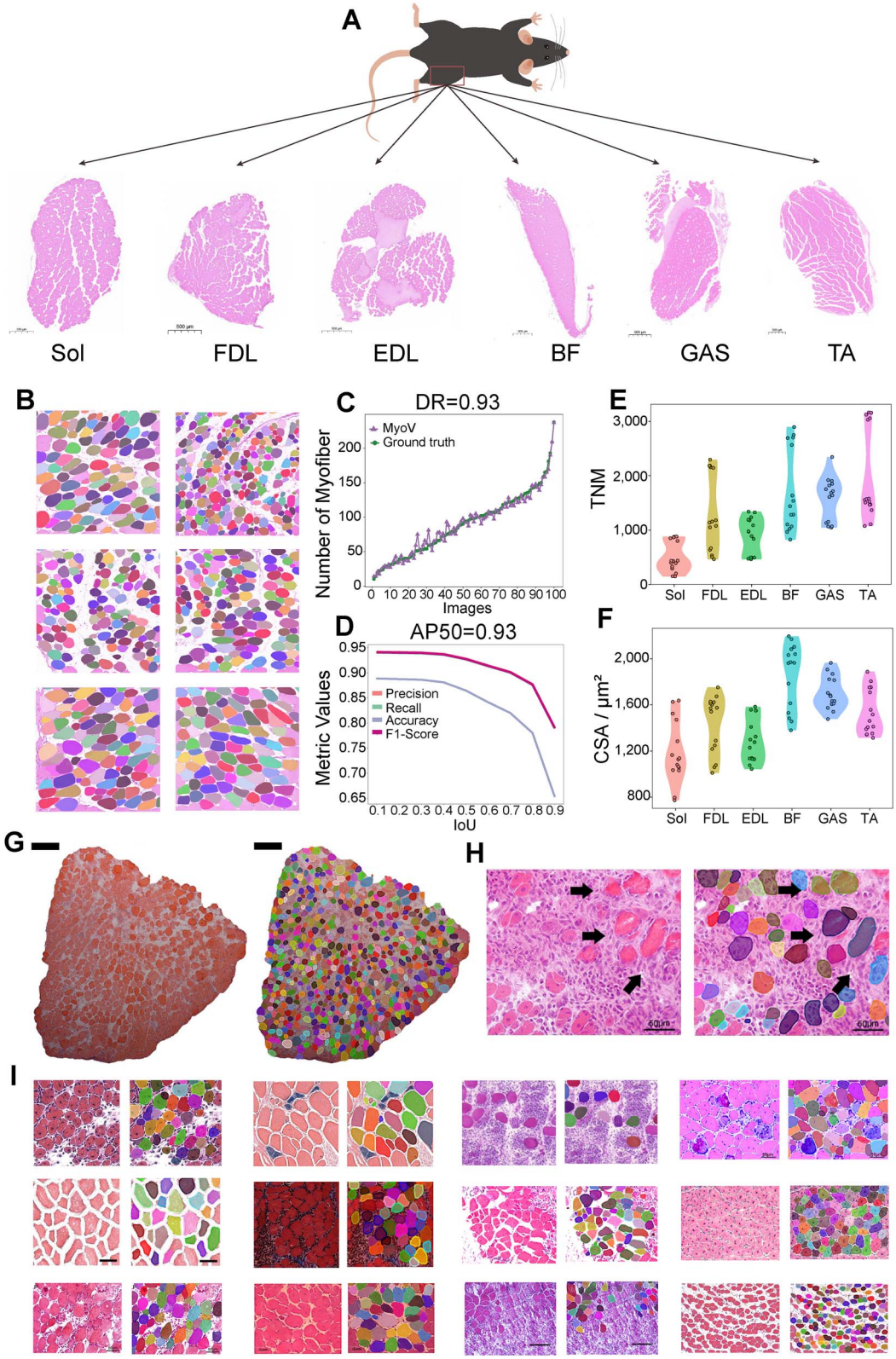

Figure 4. MyoV can be used to study muscle development in mice. (**A**) Six muscles were extracted from three mice for H&E staining. The corresponding WSIs were obtained. Sol: soleus; FDL: flexor digitorum longus; EDL: extensor digitorum longus; BF: biceps femoris; GAS: gastrocnemius; TA: tibialis anterior. (**B**) Partial visualization results obtained by MyoV detection. (**C**) DR calculated by comparing the prediction results of 100 testing images with the ground truth. (**D**) Changes in precision, recall, accuracy and F1-score values with varying IoU thresholds of testing images ($n = 100$). (**E**) TNM of the six muscles. (**F**) CSA of the muscle fibers in the six muscles. (**G**) Muscle section with Duchenne muscular dystrophy. The left side displays the original section image, while the right side shows the processed result using Model_2 of MyoV. (**H**) Muscle section after a muscle injury. The left side is the original image, while the right side is the result processed by Model_3 of MyoV. (**I**) Muscle fibers identified using Model_3 of MyoV in various stages of muscle repair after an injury and in different H&E staining conditions. The odd columns represent the original images, while the even columns represent the processed images. The mouse image was modified and drawn based on FigDraw.

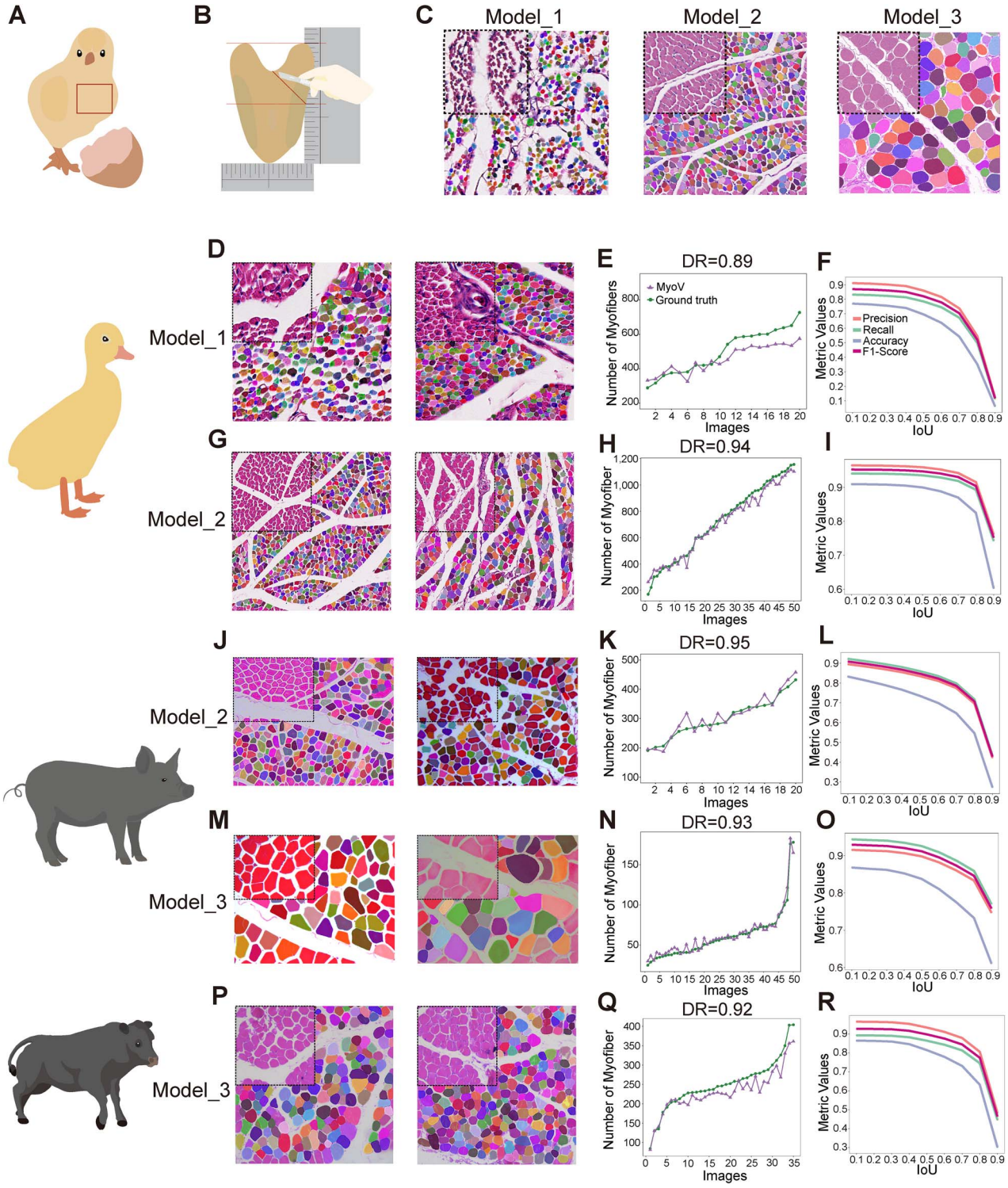

Figure 5. Improving the livestock breeding process using MyoV. (**A**) Experimental broilers used. (**B**) Procedure for obtaining a cross-section of the pectoralis major muscle. (**C**) Example results of the image tiles detected by MyoV. (**D**) Model_1 utilized to quantify the muscle fibers of the duck pectoralis major muscle. (**E**) DR achieved for 20 testing images in (**D**): 0.89 ($n = 20$). (**F**) Changes in the precision, recall, accuracy and F1-score values with varying IoU thresholds of testing images of the duck pectoralis major muscle ($n = 20$). (**G**) Model_2 utilized to quantify the muscle fibers of the duck thigh muscle. (**H**) DR achieved for 50 testing images in (**G**): 0.94. (**I**) Changes in the precision, recall, accuracy and F1-score values with varying IoU thresholds of testing images of the duck thigh muscle ($n = 50$). (**J**) Model_2 utilized to quantify the muscle fibers of the pig longissimus dorsi. (**K**) DR achieved for 20 testing images in (**J**): 0.95. (**L**) Changes in the precision, recall, accuracy and F1-score values with varying IoU thresholds of the testing images of the pig longissimus dorsi ($n = 20$). (**M**) Model_3 was utilized to quantify the muscle fibers of the pig longissimus dorsi. (**N**) DR achieved for 50 testing images in (**M**): 0.93. (**O**) Changes in the precision, recall, accuracy and F1-score values with varying IoU thresholds of the testing images of the pig longissimus dorsi ($n = 50$). (**P**) Model_3 utilized to quantify the muscle fibers of the cattle biceps femoris muscle. (**Q**) DR achieved for 35 testing images in (**P**): 0.92. (**R**) Changes in the precision, recall, accuracy and F1-score values with varying IoU thresholds of the testing images of the cattle biceps femoris muscle ($n = 35$). The pig and cattle images were modified and drawn based on FigDraw.

for precise single-cell segmentation. Cellpose is also a recently proposed deep learning-based cell segmentation method that can segment various cell types from a wide range of sources [37]. However, our experiments showed that the segmentation results of Cellpose for H&E-stained muscle fibers were unstable. Furthermore, the number of detections in Cellpose greatly fluctuated compared with the ground truth, particularly with the Model_3 test dataset. This could be attributed to Cellpose being based on the U-Net architecture design method and the training dataset not including specialized muscle slices, leading to a poor recognition of the muscle fiber cells with unclear boundaries. After completing the cell segmentation, a further quantification of the cell number, area and other indicators required the use of additional software, such as ImageJ or its plug-in LabelsToRois [63]. Developed by our team, MyoV simplified the processes of batch cutting, segmentation, counting and area statistics of panoramic slices, saving researchers valuable time in statistical analysis with a simple click of the corresponding command in the software.

Mice are frequently utilized to study muscle regeneration and atrophy, and changes in the muscle phenotype serve as an important verification method [64, 65]. MyoV can assess the total number and the CSA of the muscle fibers in different parts of normal mice. After image processing, we observed that the TNM in the TA muscle was ∼1500, which was higher than ∼1200 in the EDL muscle and 200 in the Sol muscle, indicating consistency with previous research findings [66]. Similarly, the differences in the CSAs of the muscle fibers in these three muscles were consistent with those of the previous research results with CSAs of 1100, 700 and 700 μm^2, respectively. Furthermore, the CSA of the muscle fibers in the EDL muscle was 1500 μm^2, aligning with the previous research findings [67, 68]. These findings demonstrated the effectiveness of MyoV in detecting the muscle fiber phenotype in mice. In addition, we conducted a search for relevant articles on muscle damage and analyzed the slice images using MyoV to assess its suitability in determining the muscle fibers during muscle regeneration. The results revealed that, regardless of the muscle regeneration stage, MyoV can accurately detect the muscle fibers while automatically ignoring irrelevant inflammatory cells or interstitial parts, showing that it can naturally be applied to clinical medicine research.

Precise phenotyping is crucial for genetic breeding in the field of animal husbandry. For instance, laying hen breeding requires the measurement of traits, such as egg quality [69], while broiler breeding necessitates the measurement of the meat quality [70]. The histological characteristics of muscle fibers play a crucial role in determining the meat quality [71]. However, the TNM determination is rarely studied due to its large magnitude. The small size of chickens compared to that of other domestic animals makes it relatively easy to obtain a slice containing all the muscle fibers within a muscle. Our research, however, showed that the TNM in the pectoralis major muscle was at least 300 000. Manual measurement is impractical, and estimation methods yield large errors. MyoV can accurately count the TNM and measure the CSA of muscle fibers, thereby providing a practical solution for breeding practice and solving the problem of phenotyping muscle fibers in production. In the muscle fiber phenotype studies of large domestic animals, such as pigs and cattle, scholars often use a small muscle piece to make slices [72, 73]. We achieved a precision of 0.89–0.97 through multiple species verification. The commonly used software for the identification and quantification of muscle fiber cells is ImageJ; however, the watershed function of ImageJ cannot accurately identify cells with multiple internal cracks, leading to potential errors in statistical analysis. From another perspective, issues in the production process of muscle slices, such as the excessively long fixation time, the inappropriate concentration of absolute ethanol for dehydration or complications in the staining process, can lead to internal cracks that are difficult to avoid. To address this problem, we initially cut the whole muscle slide images and enlarged them to enhance the muscle fiber visibility. The training dataset of MyoV contained a certain number of slices with more cracks, allowing our software to accurately identify the cell boundaries for segmentation and determination. However, slices with many cracks and unclear boundaries between the muscle fiber cells can still pose a challenge for MyoV in terms of making correct determinations. This tool can be applied to humans, model animals and various livestock in the future. We can increase the feature types of the dataset by using automatic labeling and manual correction methods to continuously optimize and update the model.

Although our results are quite encouraging, MyoV currently has some limitations. The muscle slices used for quantification with MyoV were H&E-stained for convenience of preparation and preservation considering the constraints of the muscle fiber formation and the muscle slice preparation. The detection and the classification of the muscle fiber types that are of interest to researchers studying muscles have not yet been evaluated. This entails different slicing staining techniques and necessitates the development of subsequent solutions by establishing additional models.

In this study, we accumulated a significant number of muscle slices and annotated them to create extensive datasets, which were then used in combination with the deep learning technology to develop an automated tool capable of detecting the muscle fibers in different animals across various ages and tissues. Overall, MyoV is an excellent tool with many parameters. It exceeds the performance of existing software in terms of quantifying the muscle histology. This tool provides a practical solution to the challenges of large-scale and accurate muscle fiber quantifications and will be useful in future research on muscle development and animal production related to meat quality.

MATERIALS AND METHODS

Experimental animals

Numerous muscle tissues from five different species were used in this study. The pectoral muscle was separately isolated from broiler chickens at D1, D7, D21, D28, D35 and D42 and Peking ducks at D1 and D7. The TA, EDL, Sol, GAS, FDL and BF were harvested from sacrificed 8-week-old male C57BL/6 mice. The longissimus dorsi muscle was isolated from Peking black swine at D160–300. The biceps femoris was collected from Angus cattle at 8 weeks of age. All experiments with chicken, duck and mice in this work were approved with guidance of the ethical regulations from the Laboratory Animal Welfare and Animal Experiment Ethics Committee of China Agricultural University (Approval Code: AW71802202-1-2).

Muscle slide preparation and panoramic scanning

After isolation, all muscle samples were fixed with 4% paraformaldehyde for 48 h at room temperature. The fixed samples were then successively subjected to a first dehydration, a first permeabilization, embedding, sectioning, section stretch, deparaffinization, rehydration, hematoxylin staining, water washing, rinsing, a second dehydration, eosin counterstaining, a third dehydration, a second permeabilization and mounting to obtain the muscle

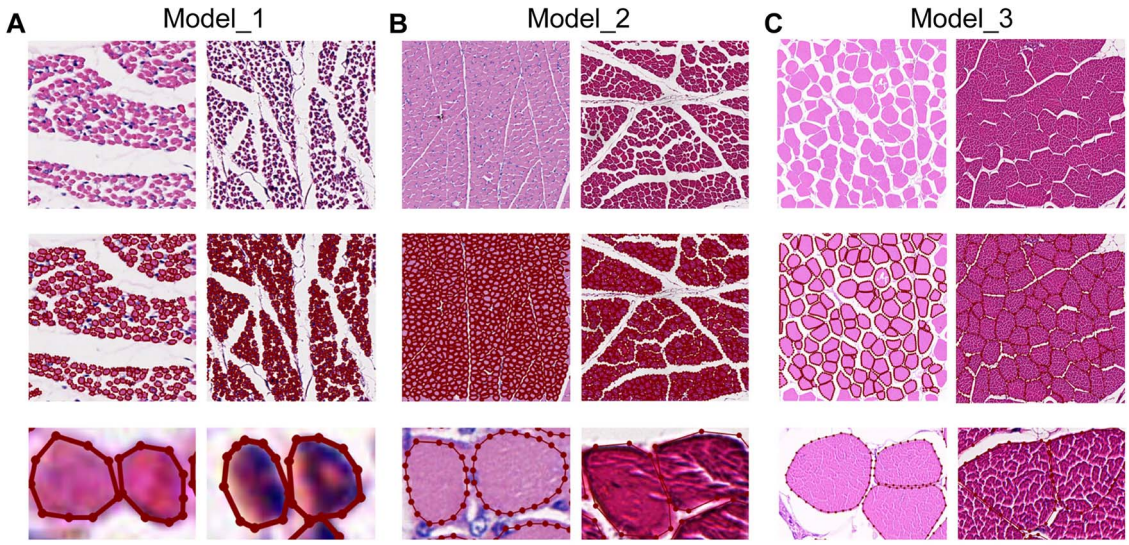

Figure 6. Labeled image tiles of the training datasets. (**A**) Example of the labeled image tiles for Model_1. The first row is the original image. The second row is the labeled image. The third row depicts the enlarged muscle fibers. *N* = 303 271 muscle fibers. (**B**) Example of the labeled image tiles for Model_2. The first row is the original image. The second row is the labeled image. The third row denotes the enlarged muscle fibers. *N* = 294 578 muscle fibers. (**C**) Example labeled image tiles for Model_3. The first row is the original image. The second row is the labeled image. The third row is the enlarged muscle fibers. *N* = 65 490 muscle fibers.

tissue slide. All slides were scanned using a Panoramic scanner (Ningbo Jiangfeng Biological Information Technology Co., Ltd. and Wuhan Service Biotechnology Co., Ltd.) and stored in SVS (.svs) and MIRAX (.mrxs) formats to obtain a high-resolution WSI that can then be stored on a computer.

Cutting of the region of interest

WSI section scanning is beneficial for visualizing the tissue morphology in biomedical research. However, it is difficult for researchers to analyze the indices of interest with the WSI using conventional methods. In this study, the regions we wanted to quantify of the WSIs were annotated with the slide analysis platform software (ASAP, ver 1.9, available as open-source software from https://github.com/computationalpathologygroup/ASAP). The WSI regions were then automatically cut into thousands of image tiles using the Python version of OpenSlide (ver 3.4.1, University of Pittsburgh, Pittsburgh, PA, https://openslide.org/).

Dataset generation

In this study, we classified the datasets into three categories according to the muscle fiber morphology and the number of muscle fibers in the image tile. The Model_1 dataset was derived from various chicken breeds at D1, a period when the muscle fiber morphology had just stabilized and was well defined. The Model_2 dataset comprised several chicken breeds sourced at D7, where the muscle fiber morphology presented high clarity, while the muscle fiber area remained comparatively small. The Model_3 dataset was composed of chickens of different breeds ranging from D21 to D42, during which period a large area of muscle fibers can be observed. At least 430 image tiles (>65 000 muscle fibers) were labeled for each category. The muscle fibers were first manually annotated by two to three annotators possessing pertinent knowledge background and foundation. An expert team with extensive experience in the observation and measurement of the muscle fibers assessed the accuracy using the LabelMe software (ver 4.6.0). In Figure 6, the muscle fibers truncated at the upper and left edges of the image tiles were labeled, while the right and lower edges were not. This approach prevented the muscle fibers from being repeatedly detected. The lower and right edges of an image tile will specifically be changed into the left and upper edges, respectively, in their adjacent image tiles; thus, they will only be marked once to maximize the precision of the muscle fiber counting of the WSIs. Preliminary models were then generated from the manually labeled datasets. We enhanced the datasets by first performing automatic labeling first using the preliminary models. The expert team then examined and labeled the insufficiently labeled muscle fibers. Three models were trained using datasets comprising 558, 430 and 600 image tiles, which corresponded to 303 271, 294 578 and 65 490 muscle fibers, respectively. We aimed to augment the quantity of the data accessible for model training, thereby improving its performance and enabling the use of a smaller test dataset. This dataset was randomly split into training and test datasets at a ratio of 7:1 [74, 75]. These datasets are available on GitHub (https://github.com/CAU-MyoV/MyoV.git).

Training procedure and configuration

The training was conducted in a Python (ver 3.6.5) runtime environment with GPU acceleration. The neural networks were programmed on the basis of PyTorch (ver 1.10.1) with two RTX3090 graphics cards. To more fully train the model, the batch size was set to 4, and the learning rate was set to 0.005 using the five default loss functions of Mask-R-CNN. The training process was iterated for 100 000 times. The learning rate was decayed at 60 000 and 80 000 iterations. The anchor size of Model_1 was set to 8, 16, 32, 64 and 128. Five anchor scales were set (i.e. 16, 32, 64, 128 and 256) to fit the datasets of Model_2 and Model_3. We diversified the training data using an augmentation method with image size randomization within a specified range, horizontal flip, vertical flip, image brightness, contrast, saturation and hue variations to improve the robustness of the trained model.

Evaluation of the MyoV accuracy

The DR is a crucial index for evaluating the counting capability of muscle fibers. It is defined as the ratio of the detected number of muscle fibers from an image tile to the ground truth. We used

the average precision (AP), recall and F1-score as the performance metrics.

DR = DN_i/GT_i.

AP = TP_i/(TP_i + FP_i).

Recall = TP_i/(TP_i + FN_i).

F1 = (2 × AP × Recall)/(AP + Recall).

DN is the detected number of the muscle fibers in image tile *i*. GT is the ground truth of the muscle fibers in image tile *i*. TP is the true positive number of the muscle fibers in image tile *i*. FP is the false-positive number of the muscle fibers in image tile *i*. FN indicates the false-negative number of the muscle fibers in image tile *i*.

Key Points

- An automated tool based on deep learning, known as MyoV, was established herein to accurately segment and quantify the hematoxylin and eosin-stained muscle fibers of whole slide images (WSIs) in various animal species.
- With MyoV, researchers can realize functions, such as sectioning, cell segmentation, area determination and automatic labeling of muscle WSIs without model retraining and parameter adjustment.
- MyoV allows muscle fiber processing with different sizes and ages and provides superior performance in quantification, surpassing both manual methods and commonly employed algorithms or software.

SUPPLEMENTARY DATA

Supplementary data are available online at http://bib.oxfordjournals.org/.

ACKNOWLEDGEMENTS

We would like to express our gratitude to Beijing Huadu Yukou Poultry Industry Co., Ltd. for their generous supply of the experimental chickens. Furthermore, we gratefully acknowledge Dr Longchao Zhang from the Institute of Animal Sciences, CASS, for generously providing the pig muscle images, and Dr Bo Wang from the College of Animal Science and Technology, China Agricultural University, for supplying the cattle muscle images. We would also like to express our gratitude to the China Agricultural University High Performance Computing Public Service Platform for computing services.

AUTHOR CONTRIBUTIONS

S.G. and C.W. contributed equally to this work. N.Y. and C.W. conceived the project and designed the research scheme. S.G. conducted the experiments with support from C.W., Z.X., H.L., Q.H., J.G., Z.J., J.L., C.S. and N.Y. S.G., C.W. and N.Y. wrote and revised the manuscript. All authors contributed to proofreading and correcting the manuscript.

FUNDING

National Key Research and Development Program of China (2022YFF1000204); National Natural Science Foundation of China (32102535); Key Research and Development Program of Hainan Province (ZDYF2023XDNY036); Program of Anhui Provincial Key Laboratory of Livestock and Poultry Product Safety Engineering.

DATA AVAILABILITY

The data that support the findings of this study are available in the supplementary material of this article. The code, GUI and datasets of MyoV are available on GitHub (https://github.com/CAU-MyoV/MyoV.git).

REFERENCES

1. Yoshioka K, Nagahisa H, Miura F, *et al.* Hoxa10 mediates positional memory to govern stem cell function in adult skeletal muscle. *Sci Adv* 2021;**7**:eabd7924.
2. Corrochano S, Männikkö R, Joyce PI, *et al.* Novel mutations in human and mouse SCN4A implicate AMPK in myotonia and periodic paralysis. *Brain* 2014;**137**:3171–85.
3. Janice SB, Tremblay AK, Leduc-Gaudet JP. Depletion of HuR in murine skeletal muscle enhances exercise endurance and prevents cancer-induced muscle atrophy. *Nat Commun* 2019;**10**:4171.
4. Cruz-Jentoft AJ, Sayer AA. Sarcopenia. *Lancet* 2019;**393**:2636–46.
5. Sui SX, Holloway-Kew KL, Hyde NK, *et al.* Handgrip strength and muscle quality in Australian women: cross-sectional data from the Geelong Osteoporosis Study. *J Cachexia Sarcopenia Muscle* 2020;**11**:690–7.
6. Wang W, Xu X, Zhang C, *et al.* Skeletal muscle fibers inspired polymeric actuator by assembly of triblock polymers. *Adv Sci (Weinh)* 2022;**9**:e2105764.
7. Lv W, Jin J, Xu Z, *et al.* lncMGPF is a novel positive regulator of muscle growth and regeneration. *J Cachexia Sarcopenia Muscle* 2020;**11**:1723–46.
8. Wang B, Guo J, Zhang M, *et al.* Insulin-degrading enzyme regulates the proliferation and apoptosis of porcine skeletal muscle stem cells via myostatin/MYOD pathway. *Front Cell Dev Biol* 2021;**9**:685593.
9. Keefe AC, Lawson JA, Flygare SD, *et al.* Muscle stem cells contribute to myofibres in sedentary adult mice. *Nat Commun* 2015;**6**:7087.
10. Costa-Verdera H, Collaud F, Riling CR, *et al.* Hepatic expression of GAA results in enhanced enzyme bioavailability in mice and non-human primates. *Nat Commun* 2021;**12**:6393.
11. Mishra P, Varuzhanyan G, Pham AH, Chan DC. Mitochondrial dynamics is a distinguishing feature of skeletal muscle fiber types and regulates organellar compartmentalization. *Cell Metab* 2015;**22**:1033–44.
12. Roman W, Martins JP, Carvalho FA, *et al.* Myofibril contraction and crosslinking drive nuclear movement to the periphery of skeletal muscle. *Nat Cell Biol* 2017;**19**:1189–201.
13. Reza MM, Subramaniyam N, Sim CM, *et al.* Irisin is a pro-myogenic factor that induces skeletal muscle hypertrophy and rescues denervation-induced atrophy. *Nat Commun* 2017;**8**:1104.
14. Liu Z, Han S, Shen X, *et al.* The landscape of DNA methylation associated with the transcriptomic network in layers and broilers generates insight into embryonic muscle development in chicken. *Int J Biol Sci* 2019;**15**:1404–18.
15. Wei X, Franke J, Ost M, *et al.* Cell autonomous requirement of neurofibromin (Nf1) for postnatal muscle hypertrophic growth and metabolic homeostasis. *J Cachexia Sarcopenia Muscle* 2020;**11**:1758–78.
16. Tajbakhsh S. Skeletal muscle stem cells in developmental versus regenerative myogenesis. *J Intern Med* 2009;**266**:372–89.

17. Markworth JF, Brown LA, Lim E, *et al.* Metabolipidomic profiling reveals an age-related deficiency of skeletal muscle pro-resolving mediators that contributes to maladaptive tissue remodeling. *Aging Cell* 2021;**20**:e13393.
18. Wang S, Zhao X, Liu Q, *et al.* Selenoprotein K protects skeletal muscle from damage and is required for satellite cells-mediated myogenic differentiation. *Redox Biol* 2022;**50**:102255.
19. Miazaki M, Viana MP, Yang Z, *et al.* Automated high-content morphological analysis of muscle fiber histology. *Comput Biol Med* 2015;**63**:28–35.
20. Lau YS, Xu L, Gao Y, Han R. Automated muscle histopathology analysis using CellProfiler. *Skelet Muscle* 2018;**8**:32.
21. Qian Y, Song J, Zhao X, *et al.* 3D fabrication with integration molding of a graphene oxide/polycaprolactone nanoscaffold for neurite regeneration and angiogenesis. *Adv Sci (Weinh)* 2018;**5**:1700499.
22. Li Y, Yang Z, Wang Y, *et al.* A neural network approach to analyze cross-sections of muscle fibers in pathological images. *Comput Biol Med* 2019;**104**:97–104.
23. Scheuermann GN, Bilgili SF, Tuzun S, Mulvaney DR. Comparison of chicken genotypes: myofiber number in pectoralis muscle and myostatin ontogeny. *Poult Sci* 2004;**83**:1404–12.
24. Huang P, Schulz TJ, Beauvais A, *et al.* Intramuscular adipogenesis is inhibited by myo-endothelial progenitors with functioning Bmpr1a signalling. *Nat Commun* 2014;**5**:4063.
25. Oksuz I, Ruijsink B, Puyol-Antón E, *et al.* Automatic CNN-based detection of cardiac MR motion artefacts using k-space data augmentation and curriculum learning. *Med Image Anal* 2019;**55**:136–47.
26. Chen L, Zeng T, Pan X, *et al.* Identifying methylation pattern and genes associated with breast cancer subtypes. *Int J Mol Sci* 2019;**20**:4269.
27. Luo Y, Mengu D, Yardimci NT, *et al.* Design of task-specific optical systems using broadband diffractive neural networks. *Light Sci Appl* 2019;**8**:112.
28. Jin L, Liu B, Zhao F, *et al.* Deep learning enables structured illumination microscopy with low light levels and enhanced speed. *Nat Commun* 2020;**11**:1934.
29. Falk T, Mai D, Bensch R, *et al.* U-Net: deep learning for cell counting, detection, and morphometry. *Nat Methods* 2019;**16**:67–70.
30. Masutani EM, Bahrami N, Hsiao A. Deep learning single-frame and multiframe super-resolution for cardiac MRI. *Radiology* 2020;**295**:552–61.
31. Fahmy AS, Neisius U, Chan RH, *et al.* Three-dimensional deep convolutional neural networks for automated myocardial scar quantification in hypertrophic cardiomyopathy: a multicenter multivendor study. *Radiology* 2020;**294**:52–60.
32. Yang Q, Xue SL, Chan CJ, *et al.* Cell fate coordinates mechano-osmotic forces in intestinal crypt formation. *Nat Cell Biol* 2021;**23**:733–44.
33. Kim J, Kim G, Li L, *et al.* Deep learning acceleration of multiscale superresolution localization photoacoustic imaging. *Light Sci Appl* 2022;**11**:131.
34. Schmidt U, Weigert M, Broaddus C. *Cell detection with star-convex polygons*. Cham, 2018;**11071**:265–73.
35. McQuin C, Goodman A, Chernyshev V, *et al.* CellProfiler 3.0: next-generation image processing for biology. *PLoS Biol* 2018;**16**:e2005970.
36. Berg S, Kutra D, Kroeger T, *et al.* Ilastik: interactive machine learning for (bio)image analysis. *Nat Methods* 2019;**16**:1226–32.
37. Stringer C, Wang T, Michaelos M, Pachitariu M. Cellpose: a generalist algorithm for cellular segmentation. *Nat Methods* 2021;**18**:100–6.
38. Gómez-de-Mariscal E, García-López-de-Haro C, Ouyang W, *et al.* DeepImageJ: a user-friendly environment to run deep learning models in ImageJ. *Nat Methods* 2021;**18**:1192–5.
39. von Chamier L, Laine RF, Jukkala J, *et al.* Democratising deep learning for microscopy with ZeroCostDL4Mic. *Nat Commun* 2021;**12**:2276.
40. Mayeuf-Louchart A, Hardy D, Thorel Q, *et al.* MuscleJ: a high-content analysis method to study skeletal muscle with a new Fiji tool. *Skelet Muscle* 2018;**8**:25.
41. Desgeorges T, Liot S, Lyon S, *et al.* Open-CSAM, a new tool for semi-automated analysis of myofiber cross-sectional area in regenerating adult skeletal muscle. *Skelet Muscle* 2019;**9**:2.
42. Stevens CR, Berenson J, Sledziona M, *et al.* Approach for semi-automated measurement of fiber diameter in murine and canine skeletal muscle. *PloS One* 2020;**15**:e243163.
43. Encarnacion-Rivera L, Foltz S, Hartzell HC, Choo H. Myosoft: an automated muscle histology analysis tool using machine learning algorithm utilizing FIJI/ImageJ software. *PloS One* 2020;**15**:e229041.
44. Rahmati M, Rashno A. Automated image segmentation method to analyse skeletal muscle cross section in exercise-induced regenerating myofibers. *Sci Rep* 2021;**11**:21327.
45. Kuru K. Optimization and enhancement of H&E stained microscopical images by applying bilinear interpolation method on lab color mode. *Theor Biol Med Model* 2014;**11**:9.
46. T. M. M., A. O. J., A. C. C. Automated histology analysis: opportunities for signal processing. *IEEE Signal Proc Mag* 2015;**32**:78–87.
47. Janssens T, Antanas L, Derde S, *et al.* Charisma: an integrated approach to automatic H&E-stained skeletal muscle cell segmentation using supervised learning and novel robust clump splitting. *Med Image Anal* 2013;**17**:1206–19.
48. He K, Gkioxari G, Dollar P, Girshick R. Mask R-CNN. *IEEE Trans Pattern Anal Mach Intell* 2020;**42**:386–97.
49. He K, Zhang X, Ren S. Deep residual learning for image recognition. *2016 IEEE Conference on Computer Vision and Pattern Recognition (CVPR)*, Las Vegas, NV, USA, 2016, 770–8.
50. Burzyn D, Kuswanto W, Kolodin D, *et al.* A special population of regulatory T cells potentiates muscle repair. *Cell* 2013;**155**:1282–95.
51. Zhu H, Hou J, Roe JL, *et al.* Amelioration of ischemia-reperfusion-induced muscle injury by the recombinant human MG53 protein. *Muscle Nerve* 2015;**52**:852–8.
52. Hardy D, Besnard A, Latil M, *et al.* Comparative study of injury models for studying muscle regeneration in mice. *PLoS One* 2016;**11**:e147198.
53. Madaro L, Passafaro M, Sala D, *et al.* Denervation-activated STAT3-IL-6 signalling in fibro-adipogenic progenitors promotes myofibres atrophy and fibrosis. *Nat Cell Biol* 2018;**20**:917–27.
54. Yue F, Bi P, Wang C, *et al.* Conditional loss of Pten in myogenic progenitors leads to postnatal skeletal muscle hypertrophy but age-dependent exhaustion of satellite cells. *Cell Rep* 2016;**17**:2340–53.
55. Spaulding HR, Ballmann CG, Quindry JC, Selsby JT. Long-term quercetin dietary enrichment partially protects dystrophic skeletal muscle. *PLoS One* 2016;**11**:e168293.
56. Millay DP, Sutherland LB, Bassel-Duby R, Olson EN. Myomaker is essential for muscle regeneration. *Genes Dev* 2014;**28**:1641–6.

57. Heier CR, Guerron AD, Korotcov A, *et al.* Non-invasive MRI and spectroscopy of mdx mice reveal temporal changes in dystrophic muscle imaging and in energy deficits. *PLoS One* 2014;**9**:e112477.
58. Saeman MR, DeSpain K, Liu MM, *et al.* Severe burn increased skeletal muscle loss in mdx mutant mice. *J Surg Res* 2016;**202**: 372–9.
59. Wang X, Zhao W, Ransohoff RM, Zhou L. Infiltrating macrophages are broadly activated at the early stage to support acute skeletal muscle injury repair. *J Neuroimmunol* 2018;**317**:55–66.
60. Yang J, Ju J, Guo L, *et al.* Prediction of HER2-positive breast cancer recurrence and metastasis risk from histopathological images and clinical information via multimodal deep learning. *Comput Struct Biotechnol J* 2022;**20**:333–42.
61. Hao F, Lee RJ, Zhong L, *et al.* Hybrid micelles containing methotrexate-conjugated polymer and co-loaded with microRNA-124 for rheumatoid arthritis therapy. *Theranostics* 2019;**9**:5282–97.
62. Xie L, Liu N, Xiao Y, *et al.* In vitro and in vivo osteogenesis induced by icariin and bone morphogenetic protein-2: a dynamic observation. *Front Pharmacol* 2020;**11**:1058.
63. Waisman A, Norris AM, Elías CM. Automatic and unbiased segmentation and quantification of myofibers in skeletal muscle. *Sci Rep* 2021;**11**:11793.
64. Chen HJ, Wang CC, Chan DC, *et al.* Adverse effects of acrolein, a ubiquitous environmental toxicant, on muscle regeneration and mass. *J Cachexia Sarcopenia Muscle* 2019;**10**:165–76.
65. Shen X, Tang J, Jiang R, *et al.* CircRILPL1 promotes muscle proliferation and differentiation via binding mir-145 to activate IGF1R/PI3K/AKT pathway. *Cell Death Dis* 2021;**12**:142.
66. Filomena MC, Yamamoto DL, Caremani M, *et al.* Myopalladin promotes muscle growth through modulation of the serum response factor pathway. *J Cachexia Sarcopenia Muscle* 2020;**11**: 169–94.
67. Goh Q, Song T, Petrany MJ, *et al.* Myonuclear accretion is a determinant of exercise-induced remodeling in skeletal muscle. *Elife* 2019;**8**:e44876.
68. Chivet M, Marchioretti C, Pirazzini M, *et al.* Polyglutamine-expanded androgen receptor alteration of skeletal muscle homeostasis and myonuclear aggregation are affected by sex, age and muscle metabolism. *Cell* 2020;**9**:325.
69. Narushin VG, Romanov MN, Mishra B, Griffin DK. Mathematical progression of avian egg shape with associated area and volume determinations. *Ann N Y Acad Sci* 2022;**1513**:65–78.
70. Shi K, Zhao Q, Shao M, *et al.* Untargeted metabolomics reveals the effect of selective breeding on the quality of chicken meat. *Metabolites* 2022;**12**:367.
71. Liu X, Du Y, Trakooljul N. Muscle transcriptional profile based on muscle fiber, mitochondrial respiratory activity, and metabolic enzymes. *Int J Biol Sci* 2015;**11**:1348–62.
72. He Q, Zou T, Chen J, *et al.* Maternal methyl-donor micronutrient supplementation during pregnancy promotes skeletal muscle differentiation and maturity in newborn and weaning pigs. *Front Nutr* 2020;**7**:609022.
73. Yu HH, Zhao H, Qing YB, *et al.* Porcine zygote injection with Cas9/sgRNA results in DMD-modified pig with muscle dystrophy. *Int J Mol Sci* 2016;**17**:1668.
74. Bobrov E, Georgievskaya A, Kiselev K, *et al.* PhotoAgeClock: deep learning algorithms for development of non-invasive visual biomarkers of aging. *Aging (Albany NY)* 2018;**10**: 3249–59.
75. Hennestad E, Witoelar A, Chambers AR, Vervaeke K. Mapping vestibular and visual contributions to angular head velocity tuning in the cortex. *Cell Rep* 2021;**37**: 110134.